ACS OMEGA

Open Access

http://pubs.acs.org/journal/acsodf

Article

Boosting Photocatalytic Activity in Rhodamine B Degradation Using Cu-Doped ZnO Nanoflakes

Jeerawan Khumphon, Ramzan Ahmed, Tanawat Imboon, Jayant Giri, Nattaporn Chattham, Faruq Mohammad, Sutasinee Kityakarn,* Veeramani Mangala Gowri,* and Sirikanjana Thongmee*

Cite This: *ACS Omega* 2025, 10, 9337−9350

Read Online

ACCESS | Metrics & More | Article Recommendations | Supporting Information

ABSTRACT: The present investigation examined how substituting some Cu^{2+} ions for Zn^{2+} ions could increase zinc oxide (ZnO) photocatalytic activity toward the reduction of Rhodamine B. Phase composition, the presence of functional groups, optical properties, emission spectra, and surface morphology of ZnO nanoflakes (NFs) were evaluated using X-ray diffraction (XRD), Fourier transform infrared spectroscopy (FT-IR), UV−visible spectroscopy (UV−vis), photoluminescence (PL) spectrophotometer, and scanning electron microscopy (SEM). To investigate the photocatalytic capabilities of Cu-doped ZnO NFs driven by visible light/sunlight, Rhodamine B dyes were photocatalytically degraded in water using UV−visible absorption spectroscopy. Using Williamson-Hall analysis of the XRD data, it was discovered that the internal strain of the Cu-doped ZnO NFs was altered. UV−vis absorption showed that the energy gap of the semiconducting ZnO NFs shrank when Cu was substituted. FT-IR studies revealed that the surface of the Cu-doped ZnO NFs contained greater amounts of reactive oxidizing species. PL studies revealed that the ZnO NFs' surface defects were being caused by the Cu substitution. According to SEM research, more surface fault NFs formed when the concentration of Cu increased. The photocatalytic activity was enhanced by the production of these NFs. The UV−vis absorption spectra showed that Cu-doped ZnO NFs were more effective than pure ZnO at degrading the rhodamine B dye (RhB). Finally, it was shown that replacing Zn^{2+} ions with Cu^{2+} ions improved the photodegradation of the rhodamine B dye. According to this study, Cu-doped ZnO NFs are an excellent choice for wastewater treatment.

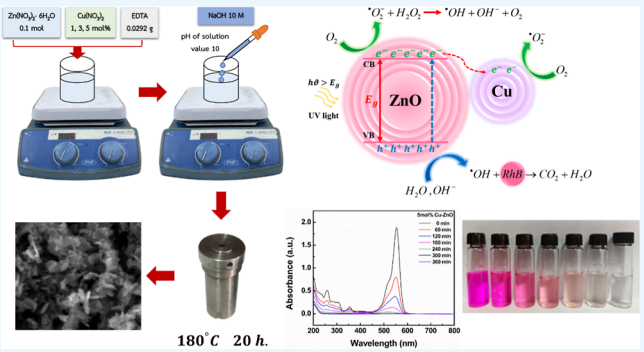

1. INTRODUCTION

Manufacturing growth has resulted in increased levels of pollution. Every year, industrial companies dump 300−400 million tons of heavy metals, solvents, toxic sludge, and other trash into the world's rivers, causing serious environmental issues. Organic pollutants include fertilizers, detergents, synthetic dyes, and heavy metals. This increase in the pollution has led to problems with the global healthcare setting.[1,2] As a result, eliminating organic contaminants is essential. Various techniques, including physical, chemical, and biological procedures, have been employed to eliminate and transform organic contaminants.[3] These methods include membrane ultrafiltration,[4,5] precipitation,[6,7] coagulation,[7,8] adsorption by activated carbon,[9,10] and reverse osmosis.[11] The fact that these treatments only change the pollutants from one phase to another means that the problems to the environment are still present.

For the elimination of organic pollutants, advanced oxidation processes (AOPs) have been utilized as an alternative to conventional treatment methods. This is because AOPs degrade harmful pollutants more cheaply and effectively in an environmentally beneficial way. Moreover, AOPs produce the potent oxidant hydroxyl radical (−OH), which is capable of fully dissolving or nonselectively mineralizing contaminants into innocuous byproducts. Among AOPs, semiconductor-mediated heterogeneous photocatalysis is a promising approach that is valuable for environmental and energy applications. Its benefits including low cost, nontoxicity, full mineralization, and reusability have caused it to become a rapidly expanding field of study in recent years. Specifically, due to their wide energy bandgap, metal semiconductors, including titanium oxide (TiO_2, 3.20 eV),[12] cadmium sulfide (CdS, 2.40 eV),[13] iron oxide (Fe_2O_3, 2.30 eV),[14] TiO_2,[15] WO_3,[16] SnO_2,[17] $SrTiO_3$,[18] and zinc oxide (ZnO, 3.37 eV),[19,20] are suited for use as photocatalysts under UV or visible light

Received: November 4, 2024
Revised: February 16, 2025
Accepted: February 20, 2025
Published: February 26, 2025

irradiation. Among these photocatalysts, TiO_2 (particularly the anatase phase) has been the subject of in-depth research on water splitting and organic pollutant degradation.[21−23] The photogenerated charge carriers from TiO_2 have a higher free energy required to form free radicals upon exposure to UV radiation. But recent research has demonstrated that ZnO is a more effective photocatalyst than TiO_2.[24−27]

Among the above metal semiconductors, ZnO is believed to have a higher efficiency in photocatalytic performance due to its higher quantum efficiency.[28−30] Furthermore, ZnO nanostructures, which have a direct band gap of about 3.37 eV, suffer from an intrinsic limitation to utilize only ∼4% of the UV portion of solar energy as a clean and safe energy source for photoexcitation in the photocatalytic process. It is employed in many different processes, such as photocatalysis, catalysis, antimicrobial products, solar cells, pharmaceuticals, and optoelectronics.[31,32] ZnO is widely employed as a photocatalyst, catalyst, and antibacterial agent because of its remarkable redox properties, biocompatibility, and lack of toxicity to living things.[33,34] Thus, efforts have been made by researchers to expand ZnO's photoresponse into the visible light spectrum, which represents around 43% of the solar spectrum.[35]

ZnO is also used in numerous other applications, such as gas sensors, transparent conducting coatings, piezoelectric transducers, and photocatalytic activity.[36] It can be synthesized with well-defined types of nanostructures such as nanotubes, nanorods, nanobelts, and nanowires.[37−39] Additionally, doping other transition metals into ZnO can enhance its optical and structural characteristics. Doping ZnO is a useful technique for enhancing photogenerated charge separation and, hence, photocatalytic efficacy. The inclusion of certain transition metals, such as Co, Mn, Fe, Cu, and Ni, has increased the photocatalytic activity of ZnO.[29,40−42] ZnO's optical and electrical properties are improved by the doping of transition metals in it.[43,44] Because Cu^{2+} (0.73) has a lower ionic radius than Zn^{2+} (0.74) and a high electrical conductivity, it is easy to penetrate the ZnO structure and alter the physical and chemical properties of ZnO.[45−47] For the synthesis of Cu-doped ZnO nanoparticles (NPs), a variety of methods have been documented in the literature, including coprecipitation, sol−gel, sonochemical synthesis, hydrothermal, solution combustion, and vapor transfer procedures.[48,49]

Cu is thought to be the most effective of them for enhancing ZnO's photocatalytic performance. Cu doping in ZnO causes major changes in its electrical, optical, and magnetic characteristics.[50−53] The visible spectrum absorbs light due to the lattice defects caused when Cu is added to ZnO, improving photocatalytic activity. The synthesis of Cu-doped ZnO microstructures was reported by Pawar et al.[54] They also demonstrated that 7% Cu-doped ZnO is required for the photocatalytic degradation of methylene blue and rhodamine B (RhB) dyes. Increased absorption of visible light, oxygen vacancies, and (001) polar surfaces were considered to be the reasons for the enhanced photocatalytic activity. Mohan et al. employed the vapor transport method to create Cu-doped ZnO nanorods, studied the photocatalytic degradation of resazurin dye under UV light, and came to the conclusion that the oxygen vacancies were what gave the Cu-doped ZnO nanorods their increased photocatalytic activity.[55] This research intended to use the hydrothermal approach to synthesize a series of ZnO compounds doped with Cu. Using scanning electron microscopy (SEM), X-ray diffraction (XRD), Fourier transform infrared spectroscopy (FT-IR), UV−visible spectroscopy (UV−vis), and photoluminescence (PL) spectroscopy, the materials' optical, structural, and chemical compositions were examined. Their photocatalytic capabilities were assessed for the degradation of RhB dye at various doping doses.

2. EXPERIMENTAL DETAILS

2.1. Synthesis of Samples. The Cu-doped ZnO nanoflakes (NFs) were prepared by a hydrothermal method. The ions in the oxide precursors can dissociate and come into close contact with one another thanks to the application of high vapor pressure and temperatures (180 °C), which speeds up the chemical reaction. When the chemical compounds were produced in an autoclave and the autoclave's temperature was lowered, the NFs precipitated out, which further reduced their solubility in the solutions. After being repeatedly washed in distilled water, the precipitates were dried for 3 h at 110 °C in an oven. Scheme S1 displays a schematic representation of the hydrothermal process. The aqueous solutions of zinc nitrate hexahydrate ($Zn(NO_3)_2{\cdot}6H_2O$) and these mixtures were shaken for 15 min after 1, 3, and 5 mol % copper(II) nitrate ($Cu(NO_3)_2$) was dissolved in 50 mL of water each. After that, 0.029 g of ethylene diamine tetra acetic acid was added to each mixture, and it was stirred for a further 15 min. Then, as NaOH was added, each mixture was constantly stirred until its pH reached 10.

The stoichiometric amounts of the precursor chemicals needed to create x mol % Cu−ZnO (x = 0, 1, 3, and 5) were measured out and dissolved in water. Each resulting mixture was put in a Teflon-lined autoclave and cooked at 180 °C for 20 h. The autoclave was then removed from the oven and allowed to reach room temperature. The nanostructure deposits within each of the cooled solutions were dried for a full day in an oven set at 60 °C after being repeatedly washed with distilled water. Ultimately, a variety of analytical methods were used to describe every sample.

2.2. Photocatalytic Activity. The photocatalytic activity of both pure ZnO and Cu-doped ZnO NFs was evaluated by causing the degradation of RhB dye in an aqueous solution using UVA (Black light), a source of sunlight. The following methodology was used to investigate the photocatalytic activity of synthesized nanomaterials under UVA (black light) irradiation from two lamps (Model: Toshiba FL40T8BL/18W). In a standard experiment, 10 mg/L of photocatalyst was mixed with 100 mL of an aqueous solution that included 10 mg/L of rhodamine B dye. After that, the combination was subjected to a UVA (black light) 2 lamp, which had a maximum emission of 470 nm and resembled sunlight. The vials containing the dye-adsorbed photocatalysts were then exposed to a light source for 0, 60, 120, 180, 240, 300, and 360 min. Before the light was turned on, the suspension of reactive RhB and the photocatalyst was shaken in the dark for 60 min to achieve a balance between adsorption and desorption. Samples were then regularly taken out of the reactor and centrifuged right away to remove any suspended materials.

3. RESULTS AND DISCUSSION

3.1. Characterization by Using Spectroscopic and Microscopic Techniques. Figure 1 displays the XRD patterns of all samples made by using the hydrothermal method with Cu Kα. These XRD patterns show the diffraction

https://doi.org/10.1021/acsomega.4c10034
ACS Omega 2025, 10, 9337−9350

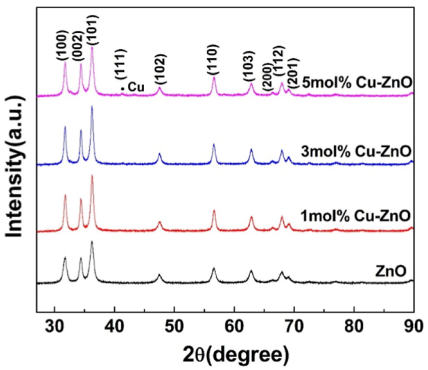

Figure 1. Cu-doped ZnO NFs and pure ZnO XRD patterns at varying concentrations (1 mol %, 3 mol %, and 5 mol %).

peaks in all samples between 2θ = 20 and 90°. The reflections in the (100), (002), (101), (102), (110), (103), (200), (112), and (201) planes are displayed in the peaks of pure ZnO, accordingly. Since they are a component of the hexagonal wurtzite structure, the peaks on the index card (JSPDS #0664) can be indexed to these.[56] The XRD patterns of Cu-doped ZnO NFs are identical to those of ZnO in the same locations, indicating that the Cu-doped ZnO NFs do not show an impurity phase at 1 mol % Cu−ZnO and maintain their wurtzite structure. The Cu peak begins to emerge in the (111) plane as the percentage of Cu grows, but its intensity is rather low, as shown in 5 mol % Cu−ZnO. The lattice parameters are computed using the standard formulas from the Miller indices for the wurtzite structure.

The sample values for lattice parameters a and c, along with the ratio c/a, are listed in Table S1. The two transition metal ions, Zn^{2+} and Co^{2+}, have been reported to have ionic radii of 0.074 and 0.073 nm, respectively.[57] A consistent decrease in the lattice parameters would result from replacing Zn^{2+} ions with only with Cu^{2+}. However, this systematic decline is not seen, as we can observe. Therefore, there is almost no change in the values as the Cu^{2+} ions replace the Zn^{2+} ions. Since the two ions' ionic diameters are comparable (0.074 nm for Zn^{2+} ions and 0.073 nm for Cu^{2+} ions), this would be expected. The presence of minimal lattice strain, which results from the small difference in ionic radii between Zn^{2+} and Cu^{2+} ions, is

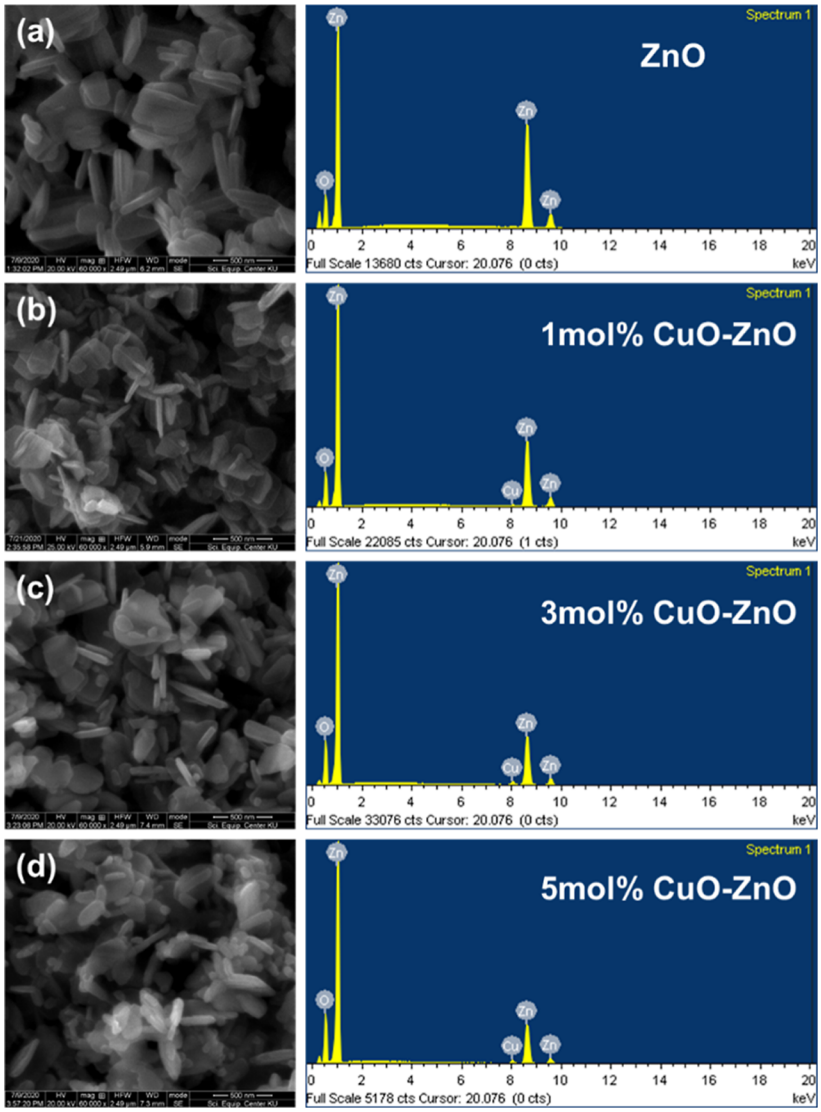

Figure 2. SEM and EDX analyses of (a) Pure ZnO NFs, (b) 1 mol % Cu-doped ZnO, (c) 3 mol % Cu-doped ZnO, and (d) 5 mol % Cu-doped ZnO.

https://doi.org/10.1021/acsomega.4c10034
ACS Omega 2025, 10, 9337−9350

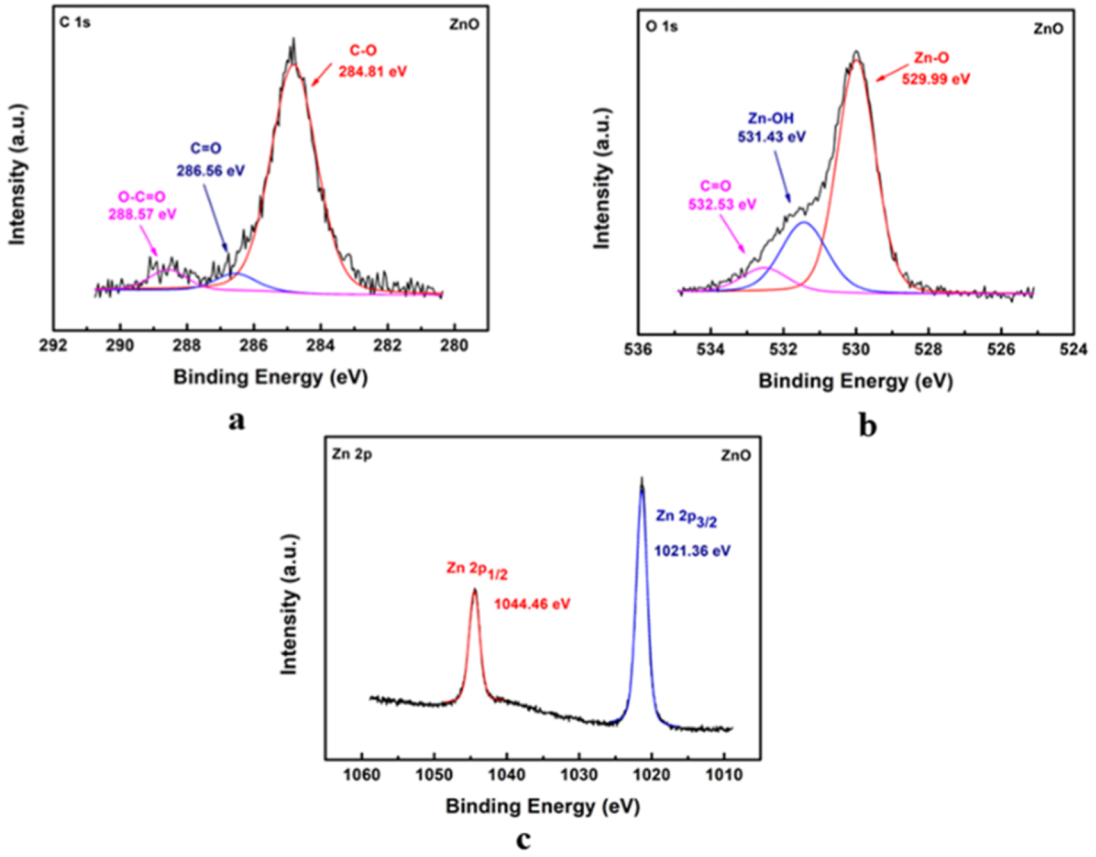

Figure 3. XPS survey and spectra of ZnO: (a) Zn C 1s, (b) Zn O 1s, and (c) Zn 2p.

suggested by the slight decrease in the a and c lattice parameters with increasing Cu doping. This lattice strain, which causes minor distortions, is the result of Zn^{2+} being substituted with Cu^{2+} in the ZnO structure. These distortions can affect the material's electronic structure, such as altering charge carrier mobility and energy band levels, which can, in turn, enhance its photocatalytic properties. Goveas et al. (2023) and Vinayagam et al. (2022) have reported similar lattice distortions caused by metal doping, confirming the notion that such alterations can enhance photocatalytic performance by enabling more effective charge separation and light absorption.[23,42]

The observed broadening of the peaks β_{hkl} present in the XRD patterns in Figure 1 can be used to determine the sizes of the NP's by use of the Scherrer–Debye formula,[40] as shown in eq 1.

$$D = \frac{K\lambda}{\beta \cos \theta} \quad (1)$$

where λ is the X-ray wavelength, θ is the diffraction angle, and K is a shape factor (usually assumed to be 0.9).

Table S1 displays the calculated values. According to the outcome, the sizes seem to be influenced by the degree of substitution. The changes do not appear to be systematic; i.e., the changes do not directly correlate with the level of Cu-substitution. The reason for the changes in the broadening of the XRD peaks is very small and subject to a great degree of uncertainty. The reason for the variation in the NFs' crystalline sizes is that as Zn ions are replaced by Cu ions, the size of the NFs first increases, then increases again as more Cu ions replace the Zn ions, and finally decreases as more Zn ions are replaced. The observed increase in crystallite size with 1% and 3% Cu doping suggests that Cu ions play a significant role in promoting grain growth within the ZnO lattice. This can be explained by the reduction in surface energy as Cu ions replace Zn^{2+} ions, which facilitates the coalescence of smaller crystallites and encourages the growth of larger grains. More uniform development is made possible by the addition of Cu ions, which probably decreases the number of defects and improves the stability of the crystal structure. On the other hand, the crystallite size somewhat shrinks as the doping amount reaches 5%. This reduction can be attributed to the increased strain and the creation of defects within the lattice caused by the higher concentration of Cu ions. Due to the mismatch in ionic radii between Cu^{2+} and Zn^{2+} ions, the lattice may become deformed at greater doping levels, which could prevent additional crystallite growth and cause more defects to emerge. These effects result in smaller crystallites at 5% Cu doping compared to the lower doping concentrations.[42]

In this study, the morphology of ZnO and Cu-doped ZnO NFs was observed by using SEM. Figure 2's images from the SEM make it abundantly evident that pure ZnO (Figure 2a) is made up of formations that resemble NFs and are usually thin, flat, and have large surface areas. The NFs maintain their structure but significantly enlarge when Cu ions are added to the ZnO lattice (Figure 2b,c). The reason for this size increase is because Cu^{2+} ions replace Zn^{2+} ions, changing the crystal structure and encouraging the formation of the NFs. The expansion of the crystalline domains is facilitated by the gradual incorporation of Cu ions into the ZnO lattice, which causes the NFs to significantly enlarge as the Cu doping concentration rises from 1 mol % to 3 mol %. However, a

https://doi.org/10.1021/acsomega.4c10034
ACS Omega 2025, 10, 9337−9350

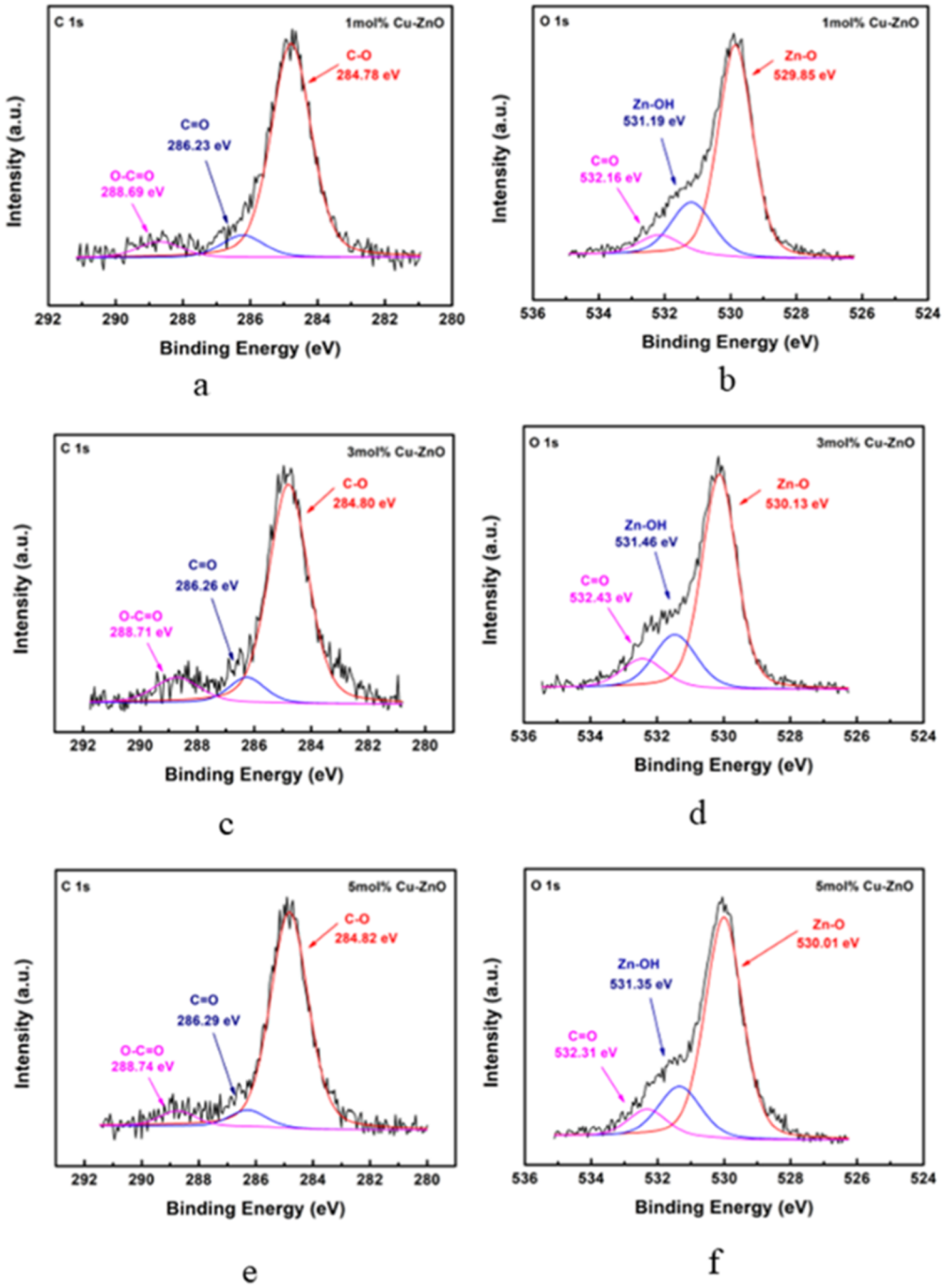

Figure 4. XPS spectra of Cu−ZnO: C 1s (a,c,e) and O 1s (b,d,f) (1, 3, and 5% Cu-doped ZnO).

reduction in size and a change in shape of the NFs are seen when the Cu doping level arrives at 5 mol % (Figure 2d). This behavior can be explained by the commencement of strain and lattice distortion brought on by the increased concentration of Cu ions, which either induces aggregation or prevents the NFs from growing further. As a result, at greater doping levels, the morphology changes, and the NFs get smaller. The material's photocatalytic qualities are directly impacted by these morphological and size changes.

The ZnO- and Cu-doped ZnO NFs EDX patterns are also shown in Figure 2. Zn, O, and Cu weight percents in ZnO NFs were found to be 90.06% and 9.94%, respectively, based on EDX analysis; for ZnO NFs that were Cu-doped, the weight percents were 84.31, 14.45, and 1.24 for 1%, 75.83, 20.68, and 3.49 for 3%, and 70.20, 25.58, and 4.22 for 5%. Zn, O, and Cu in the molecule suggest that Cu-doped ZnO NFs were developed during synthesis.

Figures 3, 4, and 5 represents the XPS spectra of ZnO, C 1s of Cu-doped ZnO (1%, 3%, and 5%), Zn 2p, and Cu 2p. Cu ion content, substitution, and value state in ZnO NFs are displayed in the XPS spectra. Furthermore, Zn^{2+} has been detected in the sample, as shown by Zn $2p_{1/2}$ and Zn $2P_{3/2}$ (1, 3, and 5%) exhibiting binding energies of 1044.35, 1044.60, and 1044.50 eV and 1021.24, 1021.50, and 1021.41 eV, respectively (Figure 5a−c).[58,59] The Cu $2p_{3/2}$ and Cu $2p_{1/2}$ core level maxima are located at 932.97 and 952.79 eV, respectively, revealing that Cu is most likely in a divalent valence state (Figure 5d).[60−62]

https://doi.org/10.1021/acsomega.4c10034
ACS Omega 2025, 10, 9337−9350

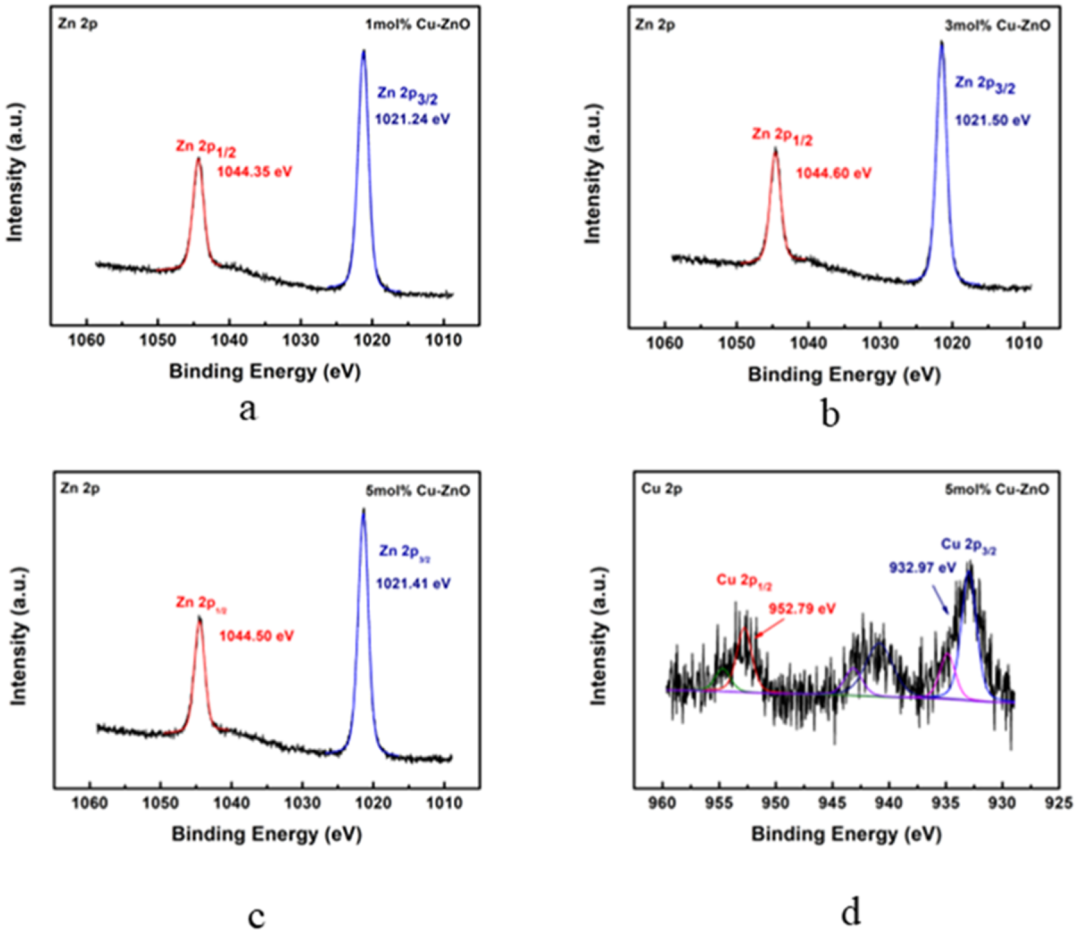

Figure 5. XPS spectra of Cu−ZnO: (a−c) Zn 2p and (d) Cu 2p.

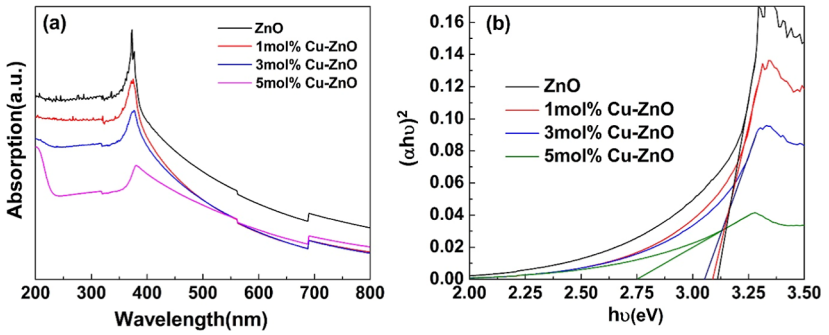

Figure 6. UV−vis spectra: (a) pure ZnO and Cu-doped ZnO (1%, 3%, and 5%) and (b) Tauc Plots.

Because Cu 2p satellite peaks are known to exist at higher binding energies and are linked to the formation of Cu 3d hole states (Cu $3d^9$), CuO (Cu^{2+}) is different from metallic copper (Cu^0) and Cu^2O (Cu^{1+}). While the 4s band of Cu_2O is empty and the 3d band is filled with (Cu $3d^{10}$), Cu^{1+} and Cu^0 show no satellite peaks.[61,62] This implies that Cu-doped ZnO NFs contain copper in its +2 valence form. Therefore, in the ZnO lattice, it is most likely that Cu^{2+} has taken the place of Zn^{2+}. Furthermore, the binding energies at 529.85, 531.19, and 532.16 eV for 1 mol % Cu−ZnO, 530.13, 531.46, and 532.43 eV for 3 mol % Cu−ZnO, and 530.01, 531.35, and 532.31 for 5 mol % Cu−ZnO are revealed by the O 1s spectra peaks, as shown in Figure 4 (b,d,f). Accordingly, the values represent oxygen vacancies and lattice oxygen (ZnO and CuO).[58,63,64]

The electronic energy gap, or the energy differential between the so-called valence band (VB) and conduction band (CB), is the most crucial property of any semiconductor. The quantum mechanical theory that the energy dispersion (E vis k) curves must have a zero slope when they pass the Brillouin boundaries results in a spectrum of prohibited energies in semiconductors. This causes a range of energies that are not related to momentum k to exist. The semiconductor can absorb light radiation only if there is an electron present that can absorb the energy and if there is an empty state into which the excited electron can enter. This definition leads to what is known as the optical band gap. The electronic band gap is somewhat larger than the optical band gap, and these two bands gap have different values. Because these investigations are easier to perform, the value of the energy gap is usually determined by

https://doi.org/10.1021/acsomega.4c10034
ACS Omega 2025, 10, 9337−9350

optical methods such as the use of a UV−vis light absorption spectrometer. Figure 6 displays the UV−visible absorption spectra of the pure ZnO and Cu-doped ZnO samples, both of which have a UV spectrum peak. It has been observed that doping ZnO with Cu increases the intensity of the UV absorption peak. Cu doping in ZnO NPs improves the efficiency of solar usage by increasing light absorption in the visible region.

In addition to the absorption spectrum, we also estimated the band gap energies from the Tauc plots.[65] The Tauc plot is the plot of $(\alpha h\nu)^2$ vs $h\nu$. Since the Tauc relationship is (eq 2)

$$(\alpha h\nu)^2 = A(h\nu - E_g) \quad (2)$$

The values of the energy gap can be obtained by linearly extrapolating the several Tauc plots. E_g. Table S2 provides the energy gap values of the Cu-doped ZnO NFs.

In preparing the NFs, the chemical reactions are carried out in water. The water molecules decompose into a proton (H^+) and a hydroxide ion $(HO)^-$. When the pH is below 7, there will be an excess of one of these ions in the water. There may also be some other ions in the solutions. Any particles generated through chemical processes can have these ions adhere to their surface. FT-IR can be used to find these. The FT-IR spectra of the three Cu-doped ZnO NFs and the pure ZnO NFs are shown in Figure 7. The dips attributed to O−H and Zn−O are noteworthy. It is observed that as more Zn ions are replaced by the Cu ions, the dips decrease, meaning there are fewer surface ions. The large peak in the FTIR spectrum at 3448 cm^{-1} is associated with the O−H stretching vibrations of hydroxyl groups, which can be caused by surface hydroxyl groups or adsorbed water molecules.[66] The existence of adsorbed water is confirmed, and a hydrophilic surface is suggested by the peak at 1633 cm^{-1}, which shows the bending vibration of H−O−H bonds.[67] The stretching vibrations of C═O functional groups are linked to the peak at 1381 cm^{-1}.[68] The wurtzite phase of ZnO is present at 568 cm^{-1}, where the peak corresponds to the Zn−O stretching vibrations. Finally, the bending vibrations of Zn−O bonds are represented by the peak at 452 cm^{-1}, which supports the ZnO framework's structural integrity.[69−78]

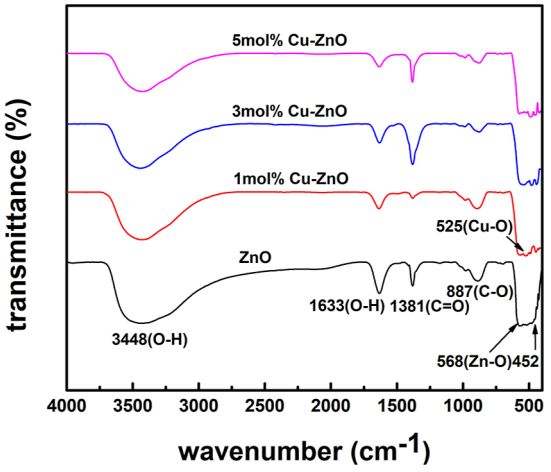

Figure 7. ZnO and Cu-doped ZnO NFs' FT-IR spectra at varying concentrations (1 mol %, 3 mol %, and 5 mol %).

3.2. Surface Area and Porosity Analysis. The surface area and porosity of pure ZnO and Cu-doped ZnO NFs were investigated by using the Brunauer−Emmett−Teller (BET) method, which yielded crucial new data regarding the structural alterations brought on by Cu doping. Pure ZnO had a BET surface area of 10.97 m^2/g, a total pore volume of 0.055 cm^3/g, and an average pore size of 21.68 nm (Table S3). The nitrogen adsorption−desorption isotherms (Figure S1) revealed Type IV isotherms, which are typical of mesoporous materials and imply a persistent porous structure with noticeable adsorption at higher relative pressures (p/p_0 > 0.8). The BET surface area rose to 12.54 m^2/g, the average pore size shrank to 19.54 nm, and the total pore volume marginally increased to 0.058 cm^3/g upon the addition of 1 mol % Cu. These changes are caused by the dispersion of Cu ions into the ZnO matrix, which enhances the porosity and decreases particle agglomeration. At 3 mol % Cu doping, however, there was a noticeable drop in the average pore size (13.03 nm), pore volume (0.012 cm^3/g), and surface area (4.21 m^2/g). This decrease is probably the consequence of the ZnO lattice being broken by excessive Cu inclusion, which leads to pore collapse and a loss of structural integrity.

Interestingly, subsequent doping at 5 mol % Cu increased the average pore size to 19.81 nm, restored the surface area to m^2/g, and increased the total pore volume to 0.040 cm^3/g. This recovery suggests that at higher doping levels, a balanced distribution of Cu ions stabilizes the lattice structure, increasing porosity and reducing agglomeration. The Type IV isotherms recorded for every sample during the investigation confirm the materials' mesoporous character. At higher relative pressures, however, variations in nitrogen adsorption are associated with variations in the surface area and pore volume. Pure ZnO and 1 mol % Cu−ZnO have higher adsorption capacities due to their bigger surface areas and porosities. In contrast, 3 mol % Cu−ZnO exhibits the lowest nitrogen uptake, which is consistent with its reduced surface area and collapsed pores. These results demonstrate the complex interplay between doping concentrations and structural qualities, highlighting the crucial role that Cu concentration plays in maximizing the material's porosity and surface properties.

3.3. Photoconversion of Surface Ions into ROS. The VB electrons in the NPs become photoexcited electrons in the CB when they absorb the radiation. They migrate inside the NPs and eventually reach the surface, where they will react with any of the O^+ or $(OH)^-$ attached to the surface to create reactive oxidizing species (ROS), such as H_2O_2, OH^-, O_2^{2-}, etc. These ROS can then oxidize and alter any other chemical compounds present in the solution. The dye RhB is the chemical compound used, as was previously said; if it were absent, the solution's color would alter. The amount of removal can be determined by recording the UV−vis light spectrum before and after the NFs are illuminated for a specific period of time. The difference will serve as a measurement of how quickly surface ions are transformed into ROS. Figure 8 depicts the variations in UV−vis light intensities after various Cu-doped ZnO NFs have been illuminated to the light for various lengths of time. The illuminations were on for 0, 60, 120, 180, 240, 300, and 360 min.

3.4. Photocatalytic Reduction Activity. In order to ascertain the photocatalytic activity for the reduction of RhB by pure ZnO and Cu-doped ZnO NFs, we first established a standard reference. This required determination of a correlation between the intensity of the absorption peak in the absorption spectrum and the quantity of RhB that emitted

https://doi.org/10.1021/acsomega.4c10034
ACS Omega 2025, 10, 9337−9350

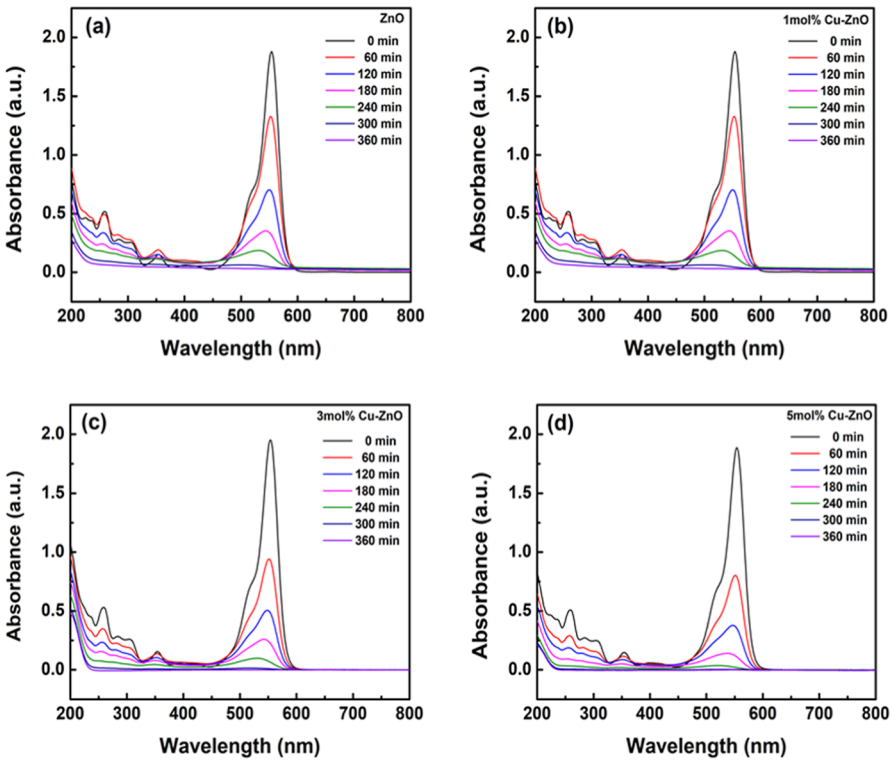

Figure 8. Rhodamine B aqueous solution UV−vis spectra at various time intervals with (a) pure ZnO NFs, (b) 1% Cu-doped, (c) 3% Cu-doped, and (d) 5% Cu-doped ZnO NFs present.

the UV−vis spectrum. After that, a steady beam of light is directed onto the solution. Five milliliters of the lighted solution was taken at various intervals (0, 60, 120, 180, 240, 300, and 360 min), and the UV−vis absorption in that sample was then measured. The findings of these measurements are shown together in Figure 8, where the intensities were measured at around 560 nm.

To perform the tests using the Cu-doped ZnO NFs in order to assess the impact of the Cu doping on the photocatalytic reduction of RhB by the ZnO NFs. The results of the present investigation are displayed in Figure 8 (b−d). We examined the absorption line at 680 nm to determine the photocatalytic reduction. The percentage of degradation by x mol % Cu−ZnO (x = 0, 1, 3, and 5) was derived from the following eq 3.

$$\%D = \frac{A_0 - A_t}{A_0} \times 100\% \tag{3}$$

where t is the reaction time, A_t is the absorbance at time t, and A_0 is the UVA light's initial absorbance at 560 nm. After determination of the percentage of degradation using the formula above, the results are shown in Figure S2. The results suggest that as the concentration of copper (Cu) in the ZnO samples increased, so did the degradation of RhB. The sample containing 5 mol % Cu−ZnO shows the most degradation compared to pure ZnO (97.32%), reaching 100% degradation after 6 h of treatment. Equation 4 provides the photocatalytic activity of Cu-doped ZnO NFs for the degradation of RhB dye based on pseudo-first-order reaction kinetics.

$$C(t) = C_0 e^{(-kt)} \tag{4}$$

where k is the rate constant. By fitting this equation to the curves in Figure S3, we found the rate constants for the Cu-free ZnO NFs, for the 1%, 3%, and 5% doped ZnO NFs to be 0.7122, 0.7493, 1.0306, and 1.2907 min^{-1}, respectively (Figure S4), while considering another relevant research in this field (Table S4). Mondal et al. report that the rate constant for ZnO NPs doped with 15% Cu was nearly twice as high as that of pure ZnO NPs.[30] The results shown in Table S2 and Figure S4 clearly illustrate that with Cu doping, the band gap energy decreases gradually, while the rate constant value increases gradually. Cu-doped ZnO NFs reduced band gap energy, leading to increased photocatalytic activity. Moreover, Cu^{2+} doping in ZnO promoted the development of more surface defects and a space charge layer, both of which are advantageous for preventing the recombination of photo-induced electron−hole pairs. Thus, the photocatalytic activity of Cu-doped ZnO NFs was higher than that of unmodified ZnO. The result of this study aligns with previous research on ZnO photocatalysts, reinforcing their effectiveness in degrading organic dyes under UV light. The crucial role of structural characteristics like surface area and crystallinity in affecting photocatalytic performance is demonstrated by comparisons with recent literature, such as Goveas et al. (2023), whose results indicate that efficient dye degradation requires high crystallinity and optimized surface area. The k value for ZnO obtained in this study is consistent with their observations, highlighting the importance of these properties.[23] Similarly, Vinayagam et al. (2022) demonstrated that doping ZnO with various elements improves degradation kinetics by enhancing charge carrier separation and broadening light absorption capabilities, further supporting the concept of structural optimization for photocatalytic efficiency.[42] In a later study, Vinayagam (2023) also emphasized that defect density and crystallinity are pivotal factors in determining ZnO's photocatalytic activity.[27] The intrinsic constraints of pure ZnO, such as greater recombination rates of photogenerated charge

https://doi.org/10.1021/acsomega.4c10034
ACS Omega 2025, 10, 9337−9350

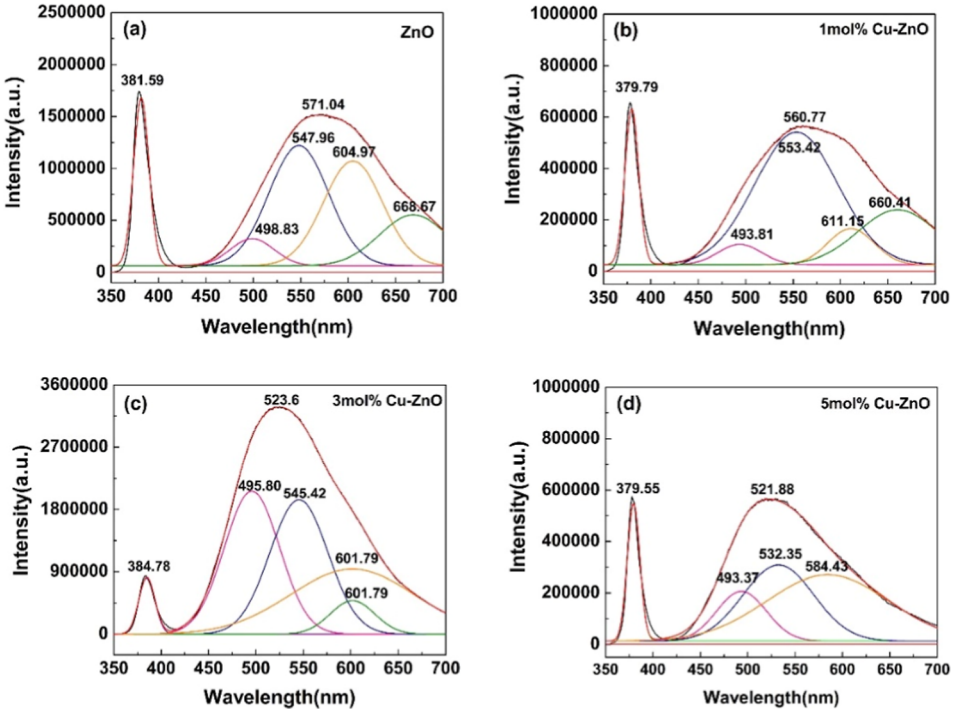

Figure 9. PL spectra: (a) pure ZnO and (b–d) Cu-doped ZnO NFs.

carriers, are the reason for the slight decrease in the k value for pure ZnO in our study when compared to doped ZnO from the literature. In spite of this, pure ZnO's similar photocatalytic effectiveness highlights its potential as an affordable, easily accessible material for environmental applications, showing that ZnO may provide notable performance in pollutant degradation even in the absence of doping.

Along with an assortment of recent research by Robkhob and colleagues,[56,79] the current study on the impact of Cu^{2+} ion replacement of Zn^{2+} ions in the ZnO NFs and the improvement of photocatalytic activity on the reduction of dyes offers insights into the photochemical behavior of NPs. The VB electrons in the NFs are excited to the CB as photoexcited electrons when they are exposed to UV light. These photoexcited electrons can catalyze the H^+ ions and the OH^- ions that were decomposed from the H_2O in the solvent into ROS such as O^{2+}, H_2O_2, or O_2^{2-}, which could be detected using FT-IR spectroscopy. These ROS can then photocatalyze any dyes or toxic ions in the solvent, thereby removing the dyes or toxic ions. Doping the ZnO NPs with Ni^{2+}, Cu^{2+}, or Li^+ ions cause a reduction of the energy gap.[80] Ref 41 provides the energy gap's strain dependency. Using a Tauc plot analysis of the UV–vis absorption curves, one can observe the decrease in photocatalytic activity as more Zn ions are exchanged out for impurity ions. To entirely comprehend the photocatalytic properties of Cu-doped ZnO NFs, further thorough experimental and theoretical research is necessary.

A strong pH dependency was observed when the influence of pH on the photocatalytic degradation efficiency of RhB was explored, as illustrated in Figures S5 and S6. In addition to 100% degradation at an acidic pH of 4.7, a maximum degradation efficiency was achieved. This was followed by 98.84% at pH 7 and 96.84% at pH 9. The superior performance at pH 4.7 is attributed to the enhanced interaction and adsorption of RhB molecules onto the photocatalyst surface in an acidic environment. On the other hand, because of electrostatic repulsion between the negatively charged photocatalyst surface and RhB molecules in an alkaline environment, the effectiveness slightly decreases at higher pH levels. These findings are consistent with earlier research on Cu and Ni dual-doped ZnO nanostructures, which have likewise demonstrated increased photocatalytic activity for the decomposition of wastewater pollutants when exposed to visible light.[81]

As no discernible degradation takes place in the absence of UV light, Figure S6 shows how pH affects the kinetics of RhB degradation under UV illumination, emphasizing the importance of UV light for photocatalytic activity. Upon UV exposure, rapid RhB degradation is observed, with the highest reduction in concentration achieved at pH 4.7, followed by pH 7 and pH 9. The increased adsorption of RhB molecules onto the photocatalyst surface and better charge carrier dynamics under acidic conditions, which promote effective photoreactions, are responsible for the higher degradation rate at pH 4.7.

Figure S7 illustrates how the Cu-doped ZnO photocatalyst's cyclic stability was assessed across five degradation cycles. The degradation efficiency was 99.62% in the first cycle and progressively fell to 98.05%, 89.42%, 81.42%, and 67.6% by the fifth cycle. This decline can be attributed to possible deactivation of the photocatalyst due to surface fouling, the accumulation of reaction intermediates, or the partial loss of active sites over repeated use.[82] The photocatalyst exhibited good stability and reusability, sustaining a fairly high degrading efficiency of 67.6% after five cycles, despite the efficiency decrease. These findings emphasize the effectiveness of Cu-doped ZnO NFs for RhB degradation under UV light. The optimal performance at acidic pH, combined with the photocatalyst's reusability, suggests its potential for practical applications in wastewater treatment and environmental remediation, offering a sustainable and efficient solution for tackling organic pollutants.

https://doi.org/10.1021/acsomega.4c10034
ACS Omega 2025, 10, 9337–9350

The stability of the photocatalyst has been proven by comparing the XRD patterns of 5 mol % Cu-doped ZnO before and after the photocatalytic degradation of RhB, as shown in Figure S8. Since there were no noticeable changes or new peaks in the diffraction peaks, the results showed that the crystalline structure and chemical integrity of Cu-doped ZnO were unaltered during the reaction. This demonstrates that the substance only served as a catalyst, accelerating the degradation process without changing its chemical state and that it did not engage in any chemical redox processes with the dye. It is possible that the photocatalyst's function was to quicken up the process without taking part in chemical transformations, further supported by the lack of other peaks. These results demonstrate Cu-doped ZnO's durability and reusability, highlighting its appropriateness for long-term environmental remediation applications.

3.5. Photoluminescence Study. Investigating PL emission aims to ascertain whether the intensity of the PL is caused by an increasing quantity of defect states and vacancies in the NFs. Djurisic et al. claim that certain kinds of flaws in ZnO's wurtzite structure are linked to energy level transitions in the emission spectrum in the visible light component of the PL spectrum.[3] It is possible to deconvolute the visible light component of the PL spectra of pure ZnO NFs acquired in this investigation into four peaks (Figure 9). The exciton peak, which is produced when the electron/hole (exciton) self-annihilates, is the sharp peak at 381.59 nm. Pure ZnO NPs' PL spectra were deconvoluted by Bhardwaj et al. using five Gaussian distributions with centers at 472, 518, 538, 591, and 628 nm.[83] Three Gaussian distributions with centers at 514, 545, and 624 nm aided in deconvoluting the PL spectrum for the 2 mol % Cu-doped ZnO NPs. Barbagiovanni et al. deconvoluted their PL spectra for their ZnO NPs with four Gaussian distributions centered at 500, 530, 580, and 630 nm.[84] According to Djurisic et al., the emissions involving the zinc vacancy defects V_{Zn} are responsible for the blue luminescence peak; the neutral and double-charged oxygen vacancies, V_O and VQ^{+2}, are responsible for the green luminescence peak; the singly ionized oxygen vacancies are responsible for the yellow luminescence peak; and the interstitial oxygen ions, O_i, on the surface of ZnO NPs are responsible for the red luminescence peak.[3]

The ZnO NFs' surface defects are crucial to their photocatalytic activity. The reason for this is that the reduction of the dyes is due to the oxidation of the dyes by the ROS created on the surface of the NFs. When the photoelectrons produced by the NFs catalysis of light absorption combine with the O^+ or OH^- to form ROS. The dye molecules (Rhodamine B dye molecules) will then be oxidized by these ROS and eliminated from the solution. We were monitoring the number of places where photo reduction processes take place while observing the red emission's intensity (Table S5).

3.6. Role of Cu-Doped ZnO nanoflakes in Photocatalysis. Figure 10 illustrates the RhB dye degradation process utilizing a Cu-doped ZnO catalyst. The ability of the photocatalyst to absorb light and generate electron−hole pairs is well recognized. The electrons were stimulated to the CB upon exposure to light irradiation. At the identical time, semiconductor holes remained in the VB.[85] After Cu doping, electron trapping inhibits electron and hole recombination in ZnO.[86−88] The photocatalyst's surface electron−hole pairs undergo a cascade of oxidation−reduction events that ultimately break down the organic pollutants. A superoxide

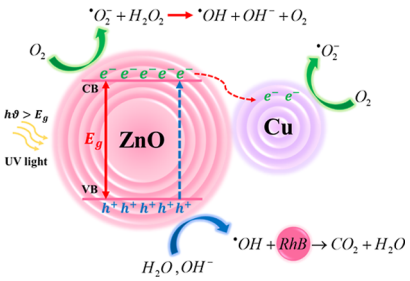

Figure 10. Possible mechanism for UV-A-induced rhodamine B degradation by the Cu-doped ZnO photocatalyst.

radical anion ($^{\bullet}O_2$) was generated when the electrons persisted on the catalyst's surface and responded with the adsorbed O_2.[89] The hydroxyl radical ($^{\bullet}OH$), which can be produced when the holes react with H_2O or −OH, can also occur. RhB dye interacts with the reactive oxygen species produced in the reaction, breaking down into less reactive intermediates such as CO_2, NH_4^+, NO_3^-, and H_2O.[90−93] This demonstrates that Cu-doped samples have more hole trapping centers, which make it easier for RhB dye molecules to absorb the photoelectron and produce byproducts. Figure 10 depicts a feasible mechanism by which the RhB dye degrades.

Cu-doped ZnO's photocatalytic process for RhB degradation works by activating a sequence of photochemical events when exposed to UV light. When UV light excites the Cu-doped ZnO, electrons (e^-) in the VB gain sufficient energy to migrate to the CB, releasing positively charged holes (h^+) in the VB. The ensuing chemical reactions are catalyzed by the electron−hole pairs produced via this mechanism. By trapping electrons and lowering recombination rates, the Cu doping improves charge separation in ZnO by introducing defect states.

The excited electrons in the CB react with oxygen molecules adsorbed on the photocatalyst surface to form $^{\bullet}O_2$.

$$O_2 + e^- \rightarrow {}^{\bullet}O_2^- \quad (5)$$

Concurrently, the VB's holes react with water (H_2O) or hydroxide ions (OH^-) to produce extremely reactive hydroxyl radicals ($^{\bullet}OH$).

$$H_2O + h^+ \rightarrow {}^{\bullet}OH + H^+ \quad (6)$$

$$HO^- + h^+ \rightarrow {}^{\bullet}OH \quad (7)$$

These ROS, including $^{\bullet}O_2^-$ and $^{\bullet}OH$, degrade RhB molecules through oxidative processes. The decomposition begins with the cleavage of the dye's chromophoric structure, leading to intermediate byproducts and eventually to complete mineralization into CO_2 and H_2O.

$$RhB + {}^{\bullet}OH/{}^{\bullet}O_2^- \rightarrow CO_2 + H_2O \quad (8)$$

By modifying its lattice structure, Cu significantly improves ZnO's photocatalytic performance. By reduction of the band gap energy, improvement of light absorption, and formation of defect sites, the addition of Cu ions makes it possible to use UV radiation for pollutant degradation more effectively. Furthermore, Cu reduces electron−hole recombination and increases photocatalytic activity by facilitating efficient charge transfer processes. Numerous studies demonstrating Cu-doped ZnO's better efficacy in degrading organic contaminants attest to these enhancements, which make it extremely beneficial for water treatment applications.

https://doi.org/10.1021/acsomega.4c10034
ACS Omega 2025, 10, 9337−9350

4. CONCLUSIONS

Cu-doped ZnO NFs were effectively synthesized in this study by using a hydrothermal process. SEM, UV−vis spectroscopy, XRD, FT-IR, BET analysis, and PL spectroscopy were used to analyze in depth the material's structural, morphological, compositional, and optical characteristics. The successful incorporation of copper ions into the ZnO lattice was validated by XRD and SEM studies. The 5% Cu-doped ZnO NFs had the best photocatalytic efficiency of all the produced samples, completely degrading RhB under UV light in 360 min. Cu was incorporated to improve the photocatalytic activity by increasing light absorption and reducing electron−hole recombination. These catalysts are very effective at reducing organic pollutants in water because of their larger surface-to-volume ratio, enhanced surface activity, and increased surface oxygen vacancies, which are all facilitated by NF morphology. Additionally, the Cu-doped ZnO NFs showed outstanding recyclability, indicating their potential for environmentally friendly wastewater treatment. Achieving optimal efficiency requires optimizing the operating parameters. Expanding this research for commercial use may provide an economical and environmentally responsible water filtration option. To further improve photocatalytic activity and investigate wider applications in photocatalytic systems, future research will be focused on developing Cu-doped ZnO materials decorated with rGO nanocomposites.

■ ASSOCIATED CONTENT

Supporting Information

The Supporting Information is available free of charge at https://pubs.acs.org/doi/10.1021/acsomega.4c10034.

Isotherms of nitrogen adsorption and desorption for both pure ZnO and Cu-doped ZnO nanofluids, proportion of pure ZnO and Cu−ZnO degradation at varying concentrations on RhB dye photocatalytic degradation at various time intervals (0, 60, 120, 180, 240, 300, and 360 min), effects of varying concentrations of pure ZnO and Cu−ZnO on RhB dye photocatalytic degradation at varying time intervals (0, 60, 120, 180, 240, 300, and 360 min), ZnO and Cu-doped ZnO rate constants, pH value's effect on RhB decomposition efficiency, pH's impact on RhB's photocatalytic breakdown, RhB dye solution photodegradation cyclic stability test, XRD patterns of 5 mol % Cu-doped ZnO prior to and following RhB's photocatalytic degradation, hydrothermal process, crystallite sizes and lattice characteristics determined using the Scherrer Formula, ZnO and Cu-doped ZnO NFs' energy bandgaps, BET method's surface area of Cu-doped ZnO NFs and pure ZnO, modified ZnO nanocatalysts used in some important studies to photocatalyze the RhB dye, and locations and regions (or intensities) of the exciton peaks and subpeaks in the visible light PL of Cu-Doped ZnO NFs and pure ZnO (PDF)

■ AUTHOR INFORMATION

Corresponding Authors

Sutasinee Kityakarn − *Department of Chemistry,Faculty of Science and Advanced Porous Materials for One Health Integrations (APM Unit), Kasetsart University, Bangkok 10900, Thailand*; Email: sutasinee.k@ku.th

Veeramani Mangala Gowri − *Department of Physics, Faculty of Science, Kasetsart University, Bangkok 10900, Thailand*; orcid.org/0000-0003-4627-3699; Email: gowrishasha1@gmail.com

Sirikanjana Thongmee − *Department of Physics, Faculty of Science, Kasetsart University, Bangkok 10900, Thailand*; orcid.org/0000-0001-8294-9997; Email: fscisjn@ku.ac.th

Authors

Jeerawan Khumphon − *Department of Physics, Faculty of Science, Kasetsart University, Bangkok 10900, Thailand*

Ramzan Ahmed − *Department of Physics, Faculty of Science, Kasetsart University, Bangkok 10900, Thailand; Department of Applied Biology, University of Science and Technology Meghalaya, Ri-Bhoi, India 793101*; orcid.org/0000-0003-3757-4764

Tanawat Imboon − *Department of Physics, Faculty of Science, Kasetsart University, Bangkok 10900, Thailand*

Jayant Giri − *Department of Mechanical Engineering, Yeshwantrao Chavan College of Engineering, Nagpur 441110, India; Division of Research and Development, Lovely Professional University, Phagwara 144411, India; Centre for Research Impact & Outcome, Chitkara University Institute of Engineering and Technology, Chitkara University, Rajpura 140401 Punjab, India*; orcid.org/0000-0003-4438-2613

Nattaporn Chattham − *Department of Physics, Faculty of Science, Kasetsart University, Bangkok 10900, Thailand*

Faruq Mohammad − *Department of Chemistry, College of Science, King Saud University, Riyadh 11451, Saudi Arabia*; orcid.org/0000-0002-9318-9986

Complete contact information is available at: https://pubs.acs.org/10.1021/acsomega.4c10034

Notes

The authors declare no competing financial interest.

■ ACKNOWLEDGMENTS

We are appreciative of the funding provided by Kasetsart University's Department of Physics, Faculty of Science. For funding under grant no. FF(KU-SRIU)11.67, S.K. and S.T. would like to express their gratitude to the Kasetsart University Research and Development Institute (KURDI). R.A. thanks the Thailand Science Research and Innovation Project and the Ministry of Higher Education, Science, Research, and Innovation for the Post-Doctoral Fellowship (ref no. 6501.0207/8434, dated August 26, 2022). The project is part of the Kasetsart University Reinventing University Program 2022. The National Research Council of Thailand (NRCT) provided funding for this study under grant number N41A640251. Additional support came from the Program Management Unit for the Human Resources & Institutional Development, Research, and Innovation (grant no. B05F640203), Kasetsart University (grant no. N42A650277), and the National Science Council of Thailand (NRCT). This research has received funding support from the National Science, Research and Innovation Fund (NSRF) via the Program Management Unit for Human Resources & Institutional Development, Research and Innovation [grant number: B13F670067]. The KSU author acknowledges funding from Researchers Supporting Project number (RSP2025R355), King Saud University, Riyadh, Saudi Arabia.

https://doi.org/10.1021/acsomega.4c10034
ACS Omega 2025, 10, 9337−9350

REFERENCES

(1) Cao, G. *Nanostructure and Nanomaterials: Synthesis Properties and Applications*; Imperial College Press: (University of Washington), 2004; p 433.
(2) Ohta, H.; Hosono, H. Transparent oxide optoelectronics. *Mater. Today* **2004**, *7* (6), 42−51.
(3) Djurišić, A. B.; Choy, W. C. H.; Roy, V. A. L.; Leung, Y. H.; Kwong, C. Y.; Cheah, K. W.; Gundu R o, T. K.; Chan, W. K.; Fei L i, H.; Surya, C. Photoluminescence and Electron Paramagnetic Resonance of ZnO Tetrapod Structures. *Adv. Funct. Mater.* **2004**, *14*, 856−864.
(4) Shinde, M. H.; Kulkarni, S. S.; Musale, D. A.; Joshi, S. G. Improvement of the water purification capability of poly(acrylonitrile) ultrafiltration membranes. *J. Membr. Sci.* **1999**, *162* (1−2), 9−22.
(5) Shen, J.; Li, D.; Jiang, F.; Qiu, J.; Gao, C. Purification and concentration of collagen by charged ultrafiltration membrane of hydrophilic polyacrylonitrile blend. *Sep. Purif. Technol.* **2009**, *66* (2), 257−262.
(6) Zhao, H.-Z.; Wang, H.-Y.; Dockko, S.; Zhang, Y. The formation mechanism of Al13 and its purification with an ethanol−acetone fractional precipitation method. *Sep. Purif. Technol.* **2011**, *81* (3), 466−471.
(7) Ndabigengesere, A.; Subba Narasiah, K. Quality of water treated by coagulation using *Moringa oleifera* seeds. *Water Res.* **1998**, *32* (3), 781−791.
(8) Mo, L.; Huanga, X. Fouling characteristics and cleaning strategies in a coagulation-microfiltration combination process for water purification. *Desalination* **2003**, *159* (1), 1−9.
(9) Spahis, N.; Addoun, A.; Mahmoudi, H.; Ghaffour, N. Purification of water by activated carbon prepared from olive stones. *Desalination* **2008**, *222* (1), 519−527.
(10) Razvigorova, M.; Budinova, T.; Petrov, N.; Minkova, V. Purification of water by activated carbons from apricot stones, lignites, and anthracite. *Water Res.* **1998**, *32* (7), 2135−2139.
(11) Baudequin, C.; Couallier, E.; Rakib, M.; Deguerry, I.; Severac, R.; Pabon, M. Purification of firefighting water containing a fluorinated surfactant by reverse osmosis coupled to electro-coagulation−filtration. *Sep. Purif. Technol.* **2011**, *76* (3), 275−282.
(12) Liu, Z.; Misra, M. Dye-Sensitized Photovoltaic Wires Using Highly Ordered TiO2 Nanotube Arrays. *ACS Nano* **2010**, *4* (4), 2196−2200.
(13) Pan, B.; Xie, Y.; Zhang, S.; Lv, L.; Zhang, W. Visible Light photocatalytic degradation of RhB by polymer-CdS nanocomposites: Role of the host functional groups. *ACS Appl. Mater. Interfaces* **2012**, *4* (8), 3938−3943.
(14) Bandara, J.; Klehm, U.; Kiwi, J. Raschig rings-Fe2O3 composite photocatalyst activate in the degradation of 4-chlorophenol and Orange II under daylight irradiation. *Appl. Catal., B* **2007**, *76* (1), 73−81.
(15) Kernazhitsky, L.; et al. Room temperature photoluminescence of anatase and rutile TiO2 powders. *J. Lumin.* **2014**, *146*, 199−204.
(16) Archana, B.; Manjunath, K.; Nagaraju, G.; Chandra Sekhar, K. B.; Kottam, N. Enhanced photocatalytic hydrogen generation and photostability of ZnO nanoparticles obtained via green synthesis. *Int. J. Hydrogen Energy* **2017**, *42* (8), 5125−5131.
(17) Leung, Y.; Xu, X.; Ma, A.; et al. Toxicity of ZnO and TiO2 to *Escherichia coli* cells. *Sci. Rep.* **2016**, *6*, 35243.
(18) Lee, K. M.; Lai, C. W.; Ngai, K. S.; Juan, J. C. Recent developments of zinc oxide based photocatalyst in water treatment technology. A review. *Water Res.* **2016**, *88*, 428−448.
(19) Velmurugan, R.; Swaminathan, M. An efficient nanostructured ZnO for dye-sensitized degradation of Reactive Red 120 dye under solar light. *Sol. Energy Mater. Sol. Cells* **2011**, *95* (3), 942−950.
(20) Ohashi, N.; Ebisawa, N.; Sekiguchi, T.; Sakaguchi, I.; Wada, Y.; Takenaka, T.; Haneda, H. Yellowish-white luminescence in codoped zinc oxide. *Appl. Phys. Lett.* **2005**, *86*, 091902.
(21) Zhuang, J.; et al. Photocatalytic Degradation of RhB over TiO2 Bilayer Films: Effect of Defects and Their Location. *Langmuir* **2010**, *26* (12), 9686−9694.
(22) Lai, C.; Sreekantana, S. Higher water splitting hydrogen generation rate for single crystalline anatase phase of TiO2 nanotube arrays. *Eur. Phys. J.:Appl. Phys.* **2012**, *59* (2), 20403.
(23) Goveas, L. C.; Nayak, S.; Vinayagam, R.; Selvaraj, R.; Pugazhendhi, A. Recent advances of Nano-photocatalysts involved in hydrogen production by water splitting. *Fuel* **2023**, *348*, 128460.
(24) Wang, G.; Chen, D.; Zhang, H.; Zhang, J.; Li, J. Tunable Photocurrent Spectrum in Well-Oriented Zinc Oxide Nanorod Arrays with Enhanced Photocatalytic Activity. *J. Phys. Chem. C* **2008**, *112*, 8850−8855.
(25) Chen, C. C. Degradation pathways of ethyl violet by photocatalytic reaction with ZnO dispersions. *J. Mol. Catal. A: Chem.* **2007**, *264* (1), 82−92.
(26) Poulios, I.; Avranas, A.; Rekliti, E.; Zouboulis, A. Photocatalytic oxidation of Auramine O in the presence of semiconducting oxides. *J. Chem. Technol. Biotechnol.* **2000**, *75* (3), 205−212.
(27) Vinayagam, R.; Pai, S.; Varadavenkatesan, T.; Pugazhendhi, A.; Selvaraj, R. Characterization and photocatalytic activity of ZnO nanoflowers synthesized using *Bridelia retusa* leaf extract. *Appl. Nanosci.* **2023**, *13*, 493−502.
(28) Srirattanapibul, S.; Tang, I.-M.; Thongmee, S. Photocatalytic reduction of Cr6+ by ZnO decorated on reduced graphene oxide (rGO) nanocomposites. *Mater. Res. Bull.* **2020**, *122*, 110705.
(29) Robkhob, P.; Ghosh, S.; Bellare, J.; Jamdade, D.; Tang, I.-M.; Thongmee, S. Effect of silver doping on antidiabetic and antioxidant potential of ZnO nanorods. *J. Trace Elem. Med. Biol.* **2020**, *58*, 126448.
(30) Mondal, S.; Ghosh, S.; Basak, D. Extraordinarily high ultraviolet photodetection by defect-tuned phosphorus-doped ZnO thin film on flexible substrate. *Mater. Res. Bull.* **2021**, *144*, 111490.
(31) Neelgund, G. M.; Oki, A. Cobalt Phthalocyanine-Sensitized Graphene−ZnO Composite: An Efficient Near-Infrared-Active Photothermal Agent. *ACS Omega* **2019**, *4* (3), 5696−5704.
(32) Kiriarachchi, H. D.; Abouzeid, K. M.; Bo, L.; El-Shall, M. S. Growth Mechanism of Sea Urchin ZnO Nanostructures in Aqueous Solutions and Their Photocatalytic Activity for the Degradation of Organic Dyes. *ACS Omega* **2019**, *4* (9), 14013−14020.
(33) Shafi, A.; Ahmad, N.; Sultana, S.; Sabir, S.; Khan, M. Z. Ag2S-Sensitized NiO−ZnO Heterostructures with Enhanced Visible Light Photocatalytic Activity and Acetone Sensing Property. *ACS Omega* **2019**, *4* (7), 12905−12918.
(34) Kahsay, M. H.; Tadesse, A.; Rama Devi, D.; Belachew, N.; Basavaiah, K. Green synthesis of zinc oxide nanostructures and investigation of their photocatalytic and bactericidal applications. *RSC Adv.* **2019**, *9* (63), 36967−36981.
(35) Ben Saad, L.; Soltane, L.; Sediri, F. Pure and Cu-Doped ZnO Nanoparticles: Hydrothermal Synthesis, Structural, and Optical Properties. *Russ. J. Phys. Chem. A* **2019**, *93*, 2782−2788.
(36) Gan, Y. X.; Jayatissa, A. H.; Yu, Z.; Chen, X.; Li, M. Hydrothermal Synthesis of Nanomaterials. *J. Nanomater.* **2020**, *2020*, 1−3.
(37) Kushnirenko, V. I.; Markevich, I. V.; Zashivailo, T. V. Acceptors related to group I elements in ZnO ceramics. *J. Lumin.* **2012**, *132* (8), 1953−1956.
(38) Kuriakose, S.; Satpati, B.; Mohapatra, S. Highly efficient photocatalytic degradation of organic dyes by Cu-doped ZnO nanostructures. *Phys. Chem. Chem. Phys.* **2015**, *17* (38), 25172−25181.
(39) Falamas, A.; Marica, I.; Popa, A.; Toloman, D.; Pruneanu, S.; Pogacean, F.; Nekvapil, F.; Silipas, T. D.; Stefan, M. Size-dependent spectroscopic insight into the steady-state and time-resolved optical properties of ZnO photocatalysts. *Mater. Sci. Semicond. Process.* **2022**, *145*, 106644.
(40) Patterson, A. L. The Scherrer Formula for X-Ray Particle Size Determination. *Phys. Rev.* **1939**, *56*, 978−982.
(41) Mote, V. D.; Purushotham, Y.; Dole, B. N. Structural morphological, physical, and dielectric properties of Mn-doped ZnO nanocrystals synthesized by sol−gel method. *Mater. Des.* **2016**, *96*, 99−105.

https://doi.org/10.1021/acsomega.4c10034
ACS Omega 2025, 10, 9337−9350

(42) Vinayagam, R.; Hebbar, A.; Senthilkumar, P.; Rangasamy, G.; Varadavenkatesan, T.; Murugesan, G.; Srivastava, S.; Concepta Goveas, L.; Manoj Kumar, N.; Selvaraj, R. Green synthesized cobalt oxide nanoparticles with photocatalytic activity towards dye removal from the water environment. *Environ. Res.* **2023**, *216*, 114766.
(43) Wang, G.; Chen, D.; Zhang, H.; Zhang, J. Z.; Li, J. Tunable Photocurrent Spectrum in Well-Oriented Zinc Oxide Nanorod Arrays with Enhanced Photocatalytic Activity. *J. Phys. Chem. C* **2008**, *112*, 8850−8855.
(44) Zhou, S. M.; Zhang, X. H.; Meng, X. M.; Zou, K.; Fan, X.; Wu, S. K.; Lee, S. T. The fabrication and optical properties of highly crystalline ultra-long Cu-doped ZnO nanowires. *Nanotechnology* **2004**, *15*, 1152−1155.
(45) Sajjad, M.; Ullah, I.; Khan, M. I.; Khan, J.; Khan, M. Y.; Qureshi, M. T. Structural and optical properties of pure and copper-doped zinc oxide nanoparticles. *Results Phys.* **2018**, *9*, 1301−1309.
(46) Prasad, N.; Saipavitra, V. M.; Swaminathan, H.; Thangaraj, P.; Viswanathan, M. R.; Balasubramanian, K. Microstress, strain, band gap tuning and photocatalytic properties of thermally annealed and Cu-doped ZnO nanoparticles. *Appl. Phys. A: Mater. Sci. Process.* **2016**, *122* (6), 590.
(47) Papadaki, D.; Mhlongo, G. H.; Motaung, D. E.; Nkosi, S. S.; Panagiotaki, K.; et al. Hierarchically Porous Cu-, Co-, and Mn-Doped Platelet-Like ZnO Nanostructures and Their Photocatalytic Performance for Indoor Air Quality Control. *ACS Omega* **2019**, *4* (15), 16429−16440.
(48) Wang, M.; Ren, F.; Cai, G.; Liu, Y.; Shen, S.; Guo, L. Activating ZnO nanorod photoanodes in visible light by Cu ion implantation. *Nano Res.* **2014**, *7* (3), 353−364.
(49) Alhadhrami, A.; Almalki, A. S.; Adam, A. M. A.; Refat, M. S. Preparation of Semiconductor Zinc Oxide Nanoparticles as a Photocatalyst to Get Rid of Organic Dyes Existing Factories in Exchange for Reuse in Suitable Purpose. *Int. J. Electrochem. Sci.* **2018**, *13*, 6503−6521.
(50) Zhou, S. M.; Zhang, X. H.; Meng, X. M.; Zou, K.; Fan, X.; Wu, S. K.; Lee, S. T. The fabrication and optical properties of highly crystalline ultra-long Cu-doped ZnO nanowires. *Nanotechnology* **2004**, *15*, 1152.
(51) Wan, W.; et al. Defects induced ferromagnetism in ZnO nanowire arrays doped with copper. *CrystEngComm* **2013**, *15* (39), 7887−7894.
(52) Sarkar, S.; Basak, D. Defect controlled ultra-high ultraviolet photocurrent gain in Cu-doped ZnO nanorod arrays: De-trapping yield. *Appl. Phys. Lett.* **2013**, *103*, 041112.
(53) Drmosh, Q. A.; Rao, S. G.; Yamani, Z. H.; Gondal, M. A. Crystalline nanostructured Cu doped ZnO thin films grown at room temperature by pulsed laser deposition technique and their characterization. *Appl. Surf. Sci.* **2013**, *270*, 104.
(54) Pawar, R. C.; Choi, D. H.; Lee, J. S.; Lee, C. S. Formation of polar surfaces in microstructured ZnO by doping with Cu and applications in photocatalysis using visible light. *Mater. Chem. Phys.* **2015**, *151*, 167−180.
(55) Mohan, R.; Krishnamoorthy, K.; Kim, S. J. Enhanced photocatalytic activity of Cu-doped ZnO nanorods. *Solid State Commun.* **2012**, *152* (5), 375−380.
(56) Daneshvar, N.; Aber, S.; Seyed Dorraji, M. S.; Khataee, A. R.; Rasoulifard, M. H. Photocatalytic degradation of the insecticide diazinon in the presence of prepared nanocrystalline ZnO powders under irradiation of UV-C light. *Sep. Purif. Technol.* **2007**, *58*, 91−98.
(57) Robkhob, P.; Tang, I. M.; Thongmee, S. Magnetic properties of the dilute magnetic semiconductor $Zn_{1-x}Co_xO$ nanoparticles. *J. Supercond. Novel Magn.* **2019**, *32*, 3637−3645.
(58) Ahmad, I.; Akhtar, M. S.; Ahmed, E.; Ahmed, M. Rare earth co-doped ZnO photocatalysts: solution combustion synthesis and environmental applications. *Sep. Purif. Technol.* **2020**, *237*, 116328.
(59) Mar, L. G.; Timbrell, P. Y.; Lamb, R. N. An XPS study of zinc oxide thin film growth on copper using zinc acetate as a precursor. *Thin Solid Films* **1993**, *223* (2), 341−347.
(60) Waskowska, A.; Gerward, L.; Olsen, J. S.; Steenstrup, S.; Talik, E. $CuMn_2O_4$ properties and the high-pressure induced Jahn-Teller phase transition. *J. Phys.: Condens. Matter* **2001**, *13* (11), 2549−2562.
(61) Pung, S. Y.; Ong, C. S.; Mohd Isha, K.; Othman, M. H. Synthesis and characterization of Cu-doped ZnO nanorods. *Sains Malays.* **2014**, *43* (2), 273−281.
(62) Pashchanka, M.; Hoffmann, R. C.; Gurlo, A.; Swarbrick, J. C.; Khanderi, J.; Engstler, J.; Issanin, A.; Schneider, J. J. A molecular approach to Cu-doped ZnO nanorods with tunable dopant content. *Dalton Trans.* **2011**, *40*, 4307−4314.
(63) Khan, M. A.; Nayan, N.; Shadiullah, S.; Ahmad, M. K.; Soon, C. F. Surface study of CuO nanopetals by advanced nanocharacterization techniques with enhanced optical and catalytic properties. *Nanomaterials* **2020**, *10* (7), 1298.
(64) Haber, J.; Stoch, J.; Ungier, L. X-ray photoelectron spectra of oxygen in oxides of Co, Ni, Fe, and Zn. *J. Electron Spectrosc. Relat. Phenom.* **1976**, *9* (5), 459−467.
(65) Tauc, J. Optical properties and electronic structure of amorphous Ge and Si. *Mater. Res. Bull.* **1968**, *3* (1), 37−46.
(66) Shashanka, R. Investigation of optical and thermal properties of CuO and ZnO nanoparticles prepared by Crocus Sativus (Saffron) flower extract. *J. Iran. Chem. Soc.* **2021**, *18* (2), 415−427.
(67) Muthukumaran, S.; Gopalakrishnan, R. Structural, FTIR and photoluminescence studies of Cu doped ZnO nanopowders by co-precipitation method. *Opt. Mater.* **2012**, *34*, 1946−1953.
(68) Jayarambabu, N.; Kumari, B.; Rao, S.; et al. Beneficial role of zinc oxide nanoparticles on green crop production. *Int. J. Adv. Multidiscip. Res.* **2015**, *10*, 273−282.
(69) Mohammed, M. K. A. Carbon nanotubes loaded ZnO/Ag ternary nanohybrid with improved visible light photocatalytic activity and stability. *Optik* **2020**, *217*, 164867.
(70) Nandi, P.; Das, D. ZnO-CuxO heterostructure photocatalyst for efficient dye degradation. *J. Phys. Chem. Solids* **2020**, *143*, 109463.
(71) Li, B.; Wang, Y. Facile synthesis and photocatalytic activity of ZnO−CuO nanocomposite. *Superlattices Microstruct.* **2010**, *47* (5), 615−623.
(72) Kumar, P. S.; Selvakumar, M.; Ganesh Babu, S.; Induja, S.; Karuthapandian, S. CuO/ZnO nanorods: An affordable efficient p-n heterojunction and morphology dependent photocatalytic activity against organic contaminants. *J. Alloys Compd.* **2017**, *701*, 562−573.
(73) Karthik, K. V.; Raghu, A. V.; Reddy, K. R.; et al. Green synthesis of Cu-doped ZnO nanoparticles and its application for the photocatalytic degradation of hazardous organic pollutants. *Chemosphere* **2022**, *287* (2), 132081.
(74) Cao, F.; Wang, T.; Ji, X. Enhanced visible photocatalytic activity of tree-like ZnO/CuO nanostructure on Cu foam. *Appl. Surf. Sci.* **2019**, *471*, 417−424.
(75) Gbair, G. A.; Alshamsi, H. A. Facile green synthesis of CuO−ZnO nanocomposites from Argyreia nervosa leaves extract for photocatalytic degradation of Rhodamine B dye. *Biomass Convers. Biorefin.* **2024**, *14*, 28117.
(76) Pal, S.; Maiti, S.; Maiti, U. N.; Chattopadhyay, K. K. Low-temperature solution-processed ZnO/CuO heterojunction photocatalyst for visible light-induced photo-degradation of organic pollutants. *CrystEngComm* **2015**, *17*, 1464−1476.
(77) Truong, T. T.; Pham, T. T.; Truong, T. T. T.; Pham, T. D. Synthesis, characterization of novel ZnO/CuO nanoparticles, and the applications in photocatalytic performance for Rhodamine B dye degradation. *Environ. Sci. Pollut. Res.* **2022**, *29*, 22576−22588.
(78) Kumari, V.; Yadav, S.; Jindal, J.; et al. Synthesis and characterization of heterogeneous ZnO/CuO hierarchical nanostructures for photocatalytic degradation of organic pollutant. *Adv. Powder Technol.* **2020**, *31* (7), 2658−2668.
(79) Robkhob, P.; Tang, I. M.; Thongmee, S. Increased bound magnetic polaron formation in the dilute magnetic semiconductor $Zn_{1-x}Ni_xO$. *Mater. Sci. Eng. B* **2020**, *260*, 114644.
(80) Tanyawong, S.; Tang, I. M.; Herng, T. S.; et al. Enhancement of virtual magnetic moment formation in ZnO NPs by Li^+ ion doping. *J. Supercond. Novel Magn.* **2020**, *33*, 2851−2859.

https://doi.org/10.1021/acsomega.4c10034
ACS Omega 2025, 10, 9337−9350

(81) Yu, J.; Bao, P.; Jin, Y.; Liu, J.; Li, J.; Lv, Y. Cu and Ni dual-doped ZnO nanostructures templated by cellulose nanofibrils with boosted visible light photocatalytic degradation of wastewater pollutants. *Green Chem.* **2023**, *25*, 10530−10537.
(82) Guo, T.; Yang, S.; Chen, Y.; et al. Photocatalytic kinetics and cyclic stability of photocatalysts Fe-complex/TiO_2 in the synergistic degradation of phenolic pollutants and reduction of Cr(VI). *Environ. Sci. Pollut. Res.* **2021**, *28*, 12459−12473.
(83) Bhardwaj, R.; Bharti, A.; Singh, J. P.; Chae, K. H.; Goyal, N. Influence of Cu doping on the local electronic and magnetic properties of ZnO nanostructures. *Nanoscale Adv.* **2020**, *2* (10), 4450−4463.
(84) Barbagiovanni, E. G.; Strano, V.; Franzò, G.; Reitano, R.; Dahiya, A. S.; Poulin-Vittrant, G.; Alquier, D.; Mirabella, S. Universal model for defect-related visible luminescence in ZnO nanorods. *RSC Adv.* **2016**, *6*, 73170−73175.
(85) Zhu, D.; Zhou, Q. Action and mechanism of semiconductor photocatalysis on degradation of organic pollutants in water treatment: A review. *Environ. Nanotechnol., Monit. Manage.* **2019**, *12*, 100255.
(86) Christy, E. J. S.; Amalraj, A.; Rajeswari, A.; Pius, A. Enhanced photocatalytic performance of Zr(IV) doped ZnO nanocomposite for the degradation efficiency of different azo dyes. *Environ. Chem. Ecotoxicol.* **2021**, *3*, 31−41.
(87) Zelekew, O. A.; Aragaw, S. G.; Sabir, F. K.; Andoshe, D. M.; Duma, A. D.; Kuo, D. H.; Chen, X.; Desissa, T. D.; Tesfamariam, B. B.; Feyisa, G. B.; et al. Green synthesis of Co-doped ZnO via the accumulation of cobalt ion onto Eichhornia crassipes plant tissue and the photocatalytic degradation efficiency under visible light. *Mater. Res. Express* **2021**, *8* (2), 025010.
(88) Zelekew, O. A.; Fufa, P. A.; Sabir, F. K.; et al. Chromium ion accumulations from aqueous solution by the Eichhornia crassipes plant and reusing in the synthesis of Cr-doped ZnO photocatalyst. *J. Nanomater.* **2022**, *10*, 4943844.
(89) Alkallas, F. H.; Ben Gouider Trabelsi, A.; Nasser, R.; Fernandez, S.; Song, J. M.; Elhouichet, H. Promising Cr-doped ZnO nanorods for photocatalytic degradation facing pollution. *Appl. Sci.* **2022**, *12*, 34.
(90) Natarajan, T. S.; Thomas, M.; Natarajan, K.; Bajaj, H. C.; Tayade, R. J. Study on UV-LED/TiO_2 process for degradation of Rhodamine B dye. *Chem. Eng. J.* **2011**, *169* (1), 126−134.
(91) Truong, T. K.; et al. Insight into the degradation of p-nitrophenol by visible-light-induced activation of peroxymonosulfate over Ag/ZnO heterojunction. *Chemosphere* **2021**, *268*, 129291.
(92) Shen, J. H.; Chiang, T. H.; Tsai, C. K.; Jiang, Z. W.; Horng, J. J. Mechanistic insights into hydroxyl radical formation of Cu-doped ZnO/g-C_3N_4 composite photocatalysis for enhanced degradation of ciprofloxacin under visible light: Efficiency, kinetics, products identification, and toxicity evaluation. *J. Environ. Chem. Eng.* **2022**, *10* (2), 107352.
(93) Truong, T. K.; Van Doan, T.; Tran, H. H.; et al. Effect of Cr doping on visible-light-driven photocatalytic activity of ZnO nanoparticles. *J. Electron. Mater.* **2019**, *48* (11), 7378−7388.

https://doi.org/10.1021/acsomega.4c10034
ACS Omega 2025, 10, 9337−9350